communications earth & environment

Article

A Nature Portfolio journal

https://doi.org/10.1038/s43247-025-02830-z

Metal scavenging by sulfide oxidation in porphyry copper deposit root zones

Shiwei Wang[1,2,3] ✉, Taofa Zhou[1], Michael Anenburg[4] ✉, Pete Hollings[2], Lejun Zhang[3], Yu Fan[1], David R. Cooke[3] & Bin Fu[4,5]

Porphyry copper (-gold) deposits in both arc and non-arc settings are hosted by oxidized magmatic rocks, but the exact mechanism by which the source magmas of these non-arc deposits become oxidized remains obscure. Through whole-rock geochemistry, mineral chemistry, and zircon isotopic analyses, here we show that the Neoproterozoic root of the Cretaceous Shaxi porphyry copper-gold deposit in the Jiangnan orogen is reduced and copper-sulfide rich, whereas the Cretaceous ore-forming magmas are oxidized. An oxidized mafic melt flushed the Neoproterozoic root zone, extracted copper and gold, and transported them to the upper crust where the Cretaceous Shaxi deposit formed. Evidence is recorded in growth zones of clinopyroxene, zircon, spinel, and plagioclase. Our results indicate that the relatively reduced, sulfide-enriched sub-continental lithospheric mantle or lower crust is essential but not sufficient for the formation of fertile non-arc porphyry magmas. Addition of a newer oxidized magma is crucial for the formation of this mineralization style.

Porphyry Cu (-Au) deposits (PCDs) typically form in oceanic subduction-related magmatic arcs, but have also been recognized in non-arc settings, including post-subduction, collisional, and intracontinental environments[1–17]. In magmatic arc settings, PCDs are the product of oceanic plate subduction, where the high metal contents (Cu, Au) and oxidation state of primitive porphyry magmas are mostly related to melt or fluid metasomatism derived from the subducted oceanic plate[18]. However, PCDs in non-arc settings are commonly considered unrelated to ongoing oceanic plate subduction, with some studies suggesting that they form through remelting of sulfide-bearing residues at the base of the crust left by earlier arc magmatism[6,8,18,19]. For example, Pettke et al.[20] used Monte Carlo simulations to infer that the Pb isotope composition of mineralizing fluid inclusions in the Cenozoic Bingham Canyon deposit was mainly derived from the subcontinental lithospheric mantle that had been metasomatized by ancient Proterozoic slab-derived fluids[21]. Core et al.[22] confirmed the existence of a Cu-rich lower crust source region beneath the Bingham deposit. Hou et al.[6] suggested that Cu–Au enriched Neoproterozoic metamorphic amphibolite xenoliths hosted by syenite and monzogranite porphyries provided the metals for the Au-rich porphyry system at the cratonic edge, based on whole-rock geochemical and zircon Hf isotopic data. However, previous studies only showed an indirect link between deeply-sourced Cu and upper crustal mineralization and did not propose oxidation and element transfer mechanisms between the deep-seated sulfide-bearing sources and the PCDs[6,8,18,23,24].

An increase in oxygen fugacity (fO_2) is generally regarded as a crucial chemical mechanism for ore-forming materials (metals, sulfur) in the sulfide-bearing residues to be dissolved and released into ascending silicate melts to form fertile non-arc PCD magmas[18,25]. Several models have been proposed to explain the increase in fO_2 that occurs in non-arc PCD magma systems, including addition of oxidized sediment during continental slab subduction[26], fractional crystallization of garnet or amphibole[27–30], gain of H_2O by basaltic replenishments and loss of H_2O during magmatic differentiation[31], or gain of oxidizing substances by interaction with high fO_2 mafic magmas[18,32]. However, the exact mechanism that oxidizes non-arc settings ore-forming magmas and subsequently releases metals from sulfide-bearing residues at the base of the crust remains unclear.

The Middle-Lower Yangtze River Valley metallogenic belt (MLYB) on the northwestern margin of the Yangtze block in South China hosts many Cretaceous PCDs (total resources >13 Mt Cu and 600 t Au). Previous studies have suggested the belt was the product of Paleo-Pacific oceanic crust subduction, but more recent work has identified it as a typical intracontinental porphyry belt that formed by partial melting of delaminated lower crust or lithospheric mantle triggered by asthenospheric upwelling[1–5,7,9–17] (Fig. 1). The MLYB occurs on the northwestern margin of the Jiangnan orogen, which was generated by subduction of the Cathaysia

[1]School of Resources and Environmental Engineering, Hefei University of Technology, Hefei, China. [2]Geology Department, Lakehead University, Thunder Bay, ON, Canada. [3]Centre for Ore Deposit and Earth Sciences (CODES), University of Tasmania, Hobart, Australia. [4]Research School of Earth Sciences, Australian National University, Canberra, Australia. [5]State Key Laboratory of Critical Mineral Research and Exploration, Institute of Geochemistry, Chinese Academy of Sciences, Guiyang, China. ✉e-mail: swwang87@hfut.edu.cn; michael.anenburg@anu.edu.au

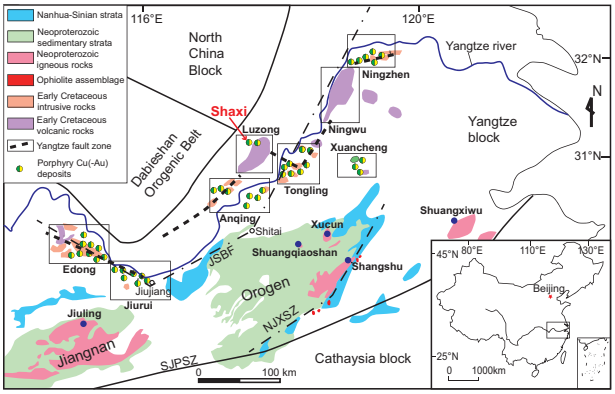

Fig. 1 | Simplified geological map of the MLYB. The map shows the location of Shaxi deposit and distribution of Neoproterozoic rocks in the Jiangnan Orogen (modified after Chen et al. and Li et al.)[3,61]. Dark blue dots show the location of Neoproterozoic rocks used as parent rock compositions for inherited zircons. SJPSZ, Shaoxing-Jiangshan-Pingxiang suture zone. NJXSZ, Northeastern Jiangxi suture zone. JSBF, the Jiujiang-Shitai buried fault (the boundary between the Yangtze carton and the Jiangnan orogen, He et al.)[85].

oceanic slab between the Cathaysia terrane and the Yangtze craton in the Early Neoproterozoic, preserving 1.1 to 0.82 Ga ophiolites, 1.1 to 0.89 Ga island arc volcanic rocks and ca. 0.87 Ga high-pressure blueschists[3,33,34] (Fig. 1). The belt was subsequently the site of shallow marine sedimentation, sporadic magmatism and high-grade metamorphism prior to the Mesozoic, covered by Jurassic-Cretaceous thick continental clastic sequences[35]. During the Late-Jurassic to Cretaceous, the belt was characterized by extensive magmatism, including felsic intrusions, bimodal volcanic rocks and A-type granites[2,3,9,36]. Ore deposits in the belt are concentrated in the eight mining districts (Edong, Jiurui, Anqing, Luzong, Tongling, Xuancheng, Ningwu, Ningzhen). PCDs primarily formed between 150 and 135 Ma, and are associated with adakitic magmas with high Sr/Y, La/Yb and low Y & Yb geochemical features[3,12,17,37].

Here, we use the Shaxi porphyry deposit, a typical PCD in the MLYB, as a case study. The Shaxi deposit (>1.5 Mt Cu at 0.55% and 40 t Au at 0.50 g/t) formed at ~129–127 Ma, slightly younger than the main metallogenic peak, and contains pre-ore diorite porphyry (DP) and syn-ore quartz diorite porphyry (QDP; Supplementary Fig. 2)[38]. Mafic enclaves have been identified in the QDP, but not in the DP (Supplementary Fig. 2). There are abundant Neoproterozoic inherited zircons and clinopyroxene xenocrysts in both the enclaves and QDP, offering a rare window into the relationship between the Cretaceous Shaxi deposit and contributions from underlying Neoproterozoic arc rocks.

Results

Whole rock geochemistry

The Shaxi intrusions have high SiO_2 (>58 wt%), Sr (>900 ppm), Sr/Y (70–160), and $(La/Yb)_N$ (12–14), and low Y (≤12.9 ppm) and Yb (≤1.2 ppm), similar to other porphyries in the MLYB (Supplementary Figs. 4-5). The mafic enclaves have high Mg# (molar 100 × Mg/(Mg+Fe), >60) with high Cr (610–650 ppm) and Ni (200–220 ppm) contents (Supplementary Table 1).

Geochronology and mineral geochemistry

Cretaceous zircons from the Shaxi DP, QDP and mafic enclaves yielded U–Pb ages of 129.3 ± 1.0 Ma, 127.0 ± 2.0 Ma and 127.6 ± 1.9 Ma, respectively (Supplementary Table 2; Supplementary Fig. 6). Inherited zircon cores were found in the DP and mafic enclaves with U–Pb ages of 811 ± 15 Ma and 804 ± 9 Ma respectively, and those in QDP yielded weighted average $^{206}Pb/^{238}U$ ages of 814 ± 10 Ma (Supplementary Fig. 6). Rare earth element (REE) patterns of the Cretaceous zircons and Neoproterozoic inherited zircons are light REE (LREE)-depleted and heavy REE (HREE)-enriched, with negative Eu anomalies, typical of igneous zircons (Fig. 2A). Oxygen fugacity was estimated following the method of Loucks et al.[39]. The calculated fO_2 (expressed as ΔFMQ, the deviation in log units from the fayalite-magnetite-quartz fO_2 buffer) for Cretaceous zircons from the DP, QDP and the mafic enclaves are ΔFMQ = +0.1 ± 0.7 (n = 14), ΔFMQ = +2.3 ± 0.6 (n = 8) and ΔFMQ = +2.3 ± 0.3 (n = 8), respectively, whereas the inherited zircon fO_2 range is ΔFMQ = −1.1 ± 1.4 (n = 11) (Fig. 2B; Supplementary Table 3).

The $\varepsilon_{Hf}(t)$ values of the Cretaceous zircon rims of the DP and QDP range from −2.7 to +0.5 (n = 16) and −2.1 to +0.6 (n = 9), those of the mafic enclaves range from −2.2 to +0.0 (n = 9), whereas the $\varepsilon_{Hf}(t)$ values of the eight Neoproterozoic inherited zircon cores vary from 0.0 to +4.6 (Fig. 2C; Supplementary Table 4). Zircon oxygen isotopic compositions of Cretaceous zircon rims from the DP are 4.44 to 6.29‰ (n = 21), the QDP are 4.95 to 6.67‰ (n = 10), and mafic enclaves are 5.61 to 6.12‰ (n = 8) (Fig. 2D). Neoproterozoic inherited zircon cores from the DP, QDP and mafic enclaves yielded oxygen isotopic compositions of 4.83 to 6.72‰ (n = 8; Supplementary Table 5).

Clinopyroxene phenocrysts (n = 5) from the mafic enclaves are zoned with cores characterized by higher SiO_2, FeO and MnO, and lower TiO_2, Al_2O_3, Cr, Co, Ni, Sr/Y and Mg# values compared to the rims (Fig. 3A, B; Supplementary Tables 6-7). Clinopyroxene cores contain abundant sulfide inclusions, consisting of pyrrhotite, pentlandite, and chalcopyrite (Fig. 3C–G; Supplementary Fig. 7; Supplementary Table 8). No sulfide inclusions were observed in clinopyroxene rims (Fig. 3A; Supplementary Fig. 7). Sulfide inclusions in clinopyroxene cores are commonly accompanied by magnetite inclusions (Supplementary Fig. 7).

Spinel from mafic enclaves generally occurs in inclusions hosted in other minerals. They are magmatically zoned, different to weathered spinel with a typical irregular shape and porous texture. The magmatic spinel cores are dominated by the chrome-spinel component, whereas the rims are predominantly chromian magnetite (Fig. 3H, Supplementary Fig. 8, Supplementary Table 9).

Apatite from DP, QDP and mafic enclaves occurs in primary inclusions as well as cleavage and fracture infill (particularly in amphibole). Here, we only consider primary apatite inclusions away from the edge and the fracture zones of magmatic minerals (Supplementary Fig. 9). Sulfate in apatites from the QDP (0.14–0.83 wt%) and mafic enclaves (0.11–0.61 wt%) is higher than DP apatite (0.03–0.16 wt%; Fig. 3I; Supplementary Table 10). All DP and QDP apatites have high Mn/Fe and LREE/HRE values indicating a magmatic origin (Supplementary Fig. 10; Supplementary Table 11)[40]. Plagioclase from the QDP has inverse zoning, characterized by oligoclase cores (An# = 22–30), mantled by andesine rims (An# = 36–45; Fig. 3K; Supplementary Table 12).

Discussion

Copper and sulfur release by interaction with oxidized mafic magma

Mafic enclaves are commonly interpreted as either (1) partial melting residues from the host magma formation, (2) xenoliths incorporated into the magma by wall rock stoping, (3) autoliths formed during parent magma crystallization representing early crystal accumulations, or (4) products of mafic magma mingling[41]. The age of the Shaxi mafic enclaves is similar to the age of the QDP, negating a xenolith origin. Morphology, magmatic textures, mineralogy, and chemical features of the Shaxi mafic enclaves indicate that they crystallized from a mafic magma. There is a diffuse fine-grained margin in the contact zone between the mafic enclaves and QDP, with clinopyroxene, plagioclase, ilmenite and other fine-grained minerals (Supplementary Fig. 2I). This suggests that these mafic enclaves are not restites. Autoliths are typically flow-microstructured with pillow-shaped chilled margins, similar mineral assemblages, higher compatible elements (Sc, V and Ni) and HREE, and lower incompatible elements (Ba, Rb, Th, U and Zr) compared with their host rocks[41]. However, at Shaxi, the contact zone between the mafic enclave and QDP has no flow microstructure or pillow-shape, and their incompatible trace element contents are higher than

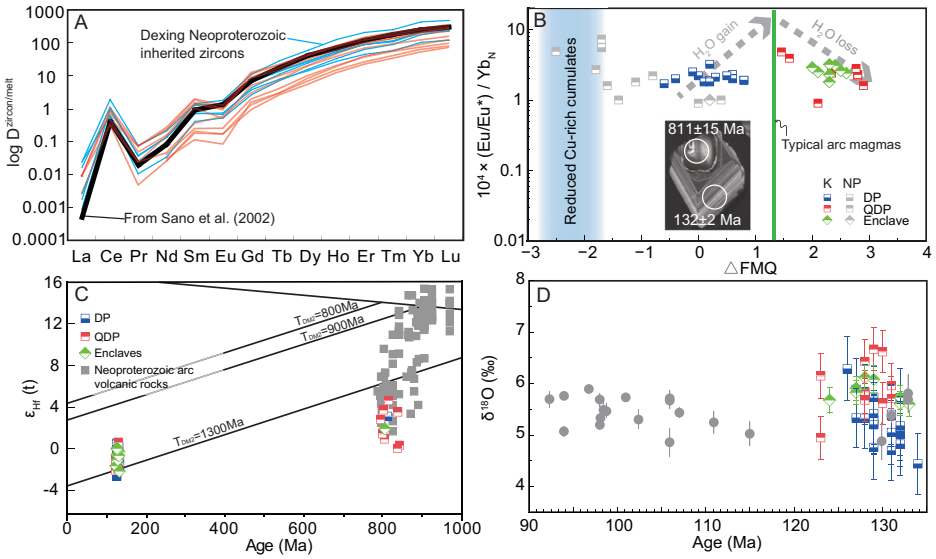

Fig. 2 | Geochemical characteristics of whole rock and zircons. A Plot of log $D^{zircon/melt}$ calculated for inherited zircons (red lines) using Shuangxiwu volcanic rocks. Dexing Neoproterozoic inherited zircons data from Zhang et al.[58], the partition coefficients (black line) for zircon are from Sano et al.[86]. **B** Calculated fO_2 vs. $10^4 \times (Eu/Eu^*)/Yb_N$. Colored symbols are Cretaceous (K) zircons, gray symbols are Neoproterozoic (NP) zircons. Reduced Cu-rich cumulates in the lower crust data from Tassara and Ague[23], the fO_2 value of typical arc magma data from Cottrell et al.[87]. **C** Lu-Hf isotopic evolution trend. Neoproterozoic volcanic arc rock zircons Lu-Hf isotopic data from Li et al.[34], Chen et al.[88], Wang et al.[57] and Yin et al.[89]. **D** $\delta^{18}O$ (‰) vs. age. Error bars refer to ±2σ (external). Zircon $\delta^{18}O$ values (Gray bar) of calc-alkaline felsic rocks in SE China refer to Xu et al.[11].

the QDP. Thus, we conclude that the mafic enclaves in the ore-bearing QDP represent mostly thermodynamically equilibrated liquids and mineral rims but poorly-mixed remnants of a mafic melt that was injected into the QDP-forming magma. Thermodynamic equilibrium is supported by similar chemical compositions of apatite, spinel rims, zircon rims, and plagioclase rims in both QDP and the enclaves. The primitive character of the mafic melt is indicated by plagioclase rims from QDP richer in the anorthite component (Fig. 3K), and clinopyroxene rims from the enclaves richer in Mg, Cr, and Ni (Fig. 3B), relative to the respective mineral cores. This bimodality in textures and chemical compositions is also observed in spinel and zircon, confirming the two-stage growth. No such textures have been found in the barren DP.

Zircon ages of the cores and rims constrain episodic zircon crystallization during the Neoproterozoic and Cretaceous (Supplementary Fig. 6). Oxygen fugacity of syn-ore QDP (ΔFMQ = +2.3 ± 0.6) is higher than that of the pre-ore DP (ΔFMQ = +0.1 ± 0.7) and Neoproterozoic inherited zircons (ΔFMQ = −1.1 ± 1.4; Fig. 2B), indicating that high oxidation states were present during ore formation. In the enclaves, spinel rim compositions have a substantial magnetite component, whereas the cores are primarily chrome-spinel. This indicates an abundant supply of Fe^{3+} from the deep-sourced mafic melt, compared to the more reduced cores[42]. Although a transition from chrome-spinel to magnetite could result from the stability of other aluminous phases, in Shaxi plagioclase is stable throughout so magnetite rims indicate a true oxidative effect[42].

Apatite sulfur content is an oxygen fugacity indicator of the melt[43,44], because S partitioning into apatite is strongly dependent on the melt S valence, but mostly independent of temperature and pressure[45]. Although no growth zones were observed in apatite, apatites from the ore-bearing QDP (0.14–0.83 wt%) and its mafic enclaves (0.11–0.61 wt%) have higher SO_3 content than apatite from the barren DP (0.03–0.16 wt%), which has no associated mafic enclaves (Fig. 3I). These geochemical features are interpreted to indicate an increase in fO_2 during the formation of the Shaxi ore-forming QDP magmas, relative to earlier melts.

Petrographic observations show that sulfide inclusions are only present within the cores of enclave-hosted clinopyroxene (Fig. 3A; Supplementary Fig. 7). Most sulfide inclusions are composed of shrinkage bubbles, Ti-magnetite or ilmenite, and base metal sulfides (Fig. 3E–G; Supplementary Fig. 7). Hydrothermal sulfides are mostly zoned with a spongy or vesicular texture, and commonly occur in cracks and veins with other low temperature hydrothermal minerals (e.g., hematite, chlorite)[46]. At Shaxi, hydrothermal sulfides are pyrite, chalcopyrite, and bornite, which coexist with hydrothermal minerals such as quartz, anhydrite, K-feldspar, and chlorite[38]. In contrast, we observe that sulfide inclusions are magmatic, supported by their globular or elliptical shape, lack of intersection by fractures, and complete envelopment by clinopyroxene cores (Fig. 3E–G; Supplementary Fig. 7). Base metal sulfides consist of pyrrhotite, pentlandite and chalcopyrite, with flame-structured pentlandite generally occurring in pyrrhotite (Fig. 3A, Supplementary Fig. 7), typical for magmatic sulfide inclusions[46]. The sulfides ($n = 98$) hosted in the clinopyroxene cores from mafic enclaves have high Co and Ni content, which is obviously different from hydrothermal sulfides (Supplementary Fig. 11; Supplementary Table 8). Further support for their magmatic origin comes from temperature and pressure estimations of clinopyroxene cores using the thermobarometer of Putirka[47]. These estimations are plotted in the transition zone of sulfide liquidus and monosulfide solid solution (mss) in Supplementary Fig. 12. Therefore, we consider that these sulfide inclusions are of high-temperature magmatic origin, initially trapped in clinopyroxene cores as either mss or liquid during sulfide saturation.

Sulfide inclusions are absent from clinopyroxene rims. It is possible that the cores may have been xenocrysts that provided nuclei for the growth of the rims in a younger mafic magma of distinct composition. Unlike plagioclase, zircon, and spinel, where rims appear as smooth overgrowths around the mineral cores, the clinopyroxene rims are highly irregular, indicating some dissolution. These dissolution textures commonly penetrate into the cores, replacing them (Fig. 3A) with rim compositions. This replacement process probably dissolved many sulfide inclusions, while oxidizing the sulfide to sulfate (as recorded by apatite and zircon fO_2 values), and releasing Cu so that it was available for subsequent mineralization.

Subduction of oxidized sediment on continental slabs could increase fO_2 in non-arc PCD magmas[26]. However, the adakitic Shaxi intrusive rocks are different from the products of subducted oceanic crust-derived adakites, similar to thick lower crust-derived adakite-like rocks (Fig. 4A, B). Additional geochemical and geophysical evidence also suggests that Cretaceous magmatism in the MLYB was formed in an intracontinental setting, driven by lithospheric thinning or delamination in response to far-field stresses at plate margins associated with the initial subduction of the paleo-Pacific plate[1–5,7,9–17].

In alternative interpretations, fO_2 increase is commonly inferred to result from garnet fractionation[27–30]. However, the DP and QDP samples display similar spoon-shaped REE patterns and lack obvious Eu anomalies, indicating dominant amphibole and minor garnet fractionation, with no evidence for plagioclase fractionation (Supplementary Figs. 4-5)[48–50]. This suggests that garnet fractionation had little impact on fO_2 increase. The pre-ore DP and syn-ore QDP have similar REE patterns, and both contain

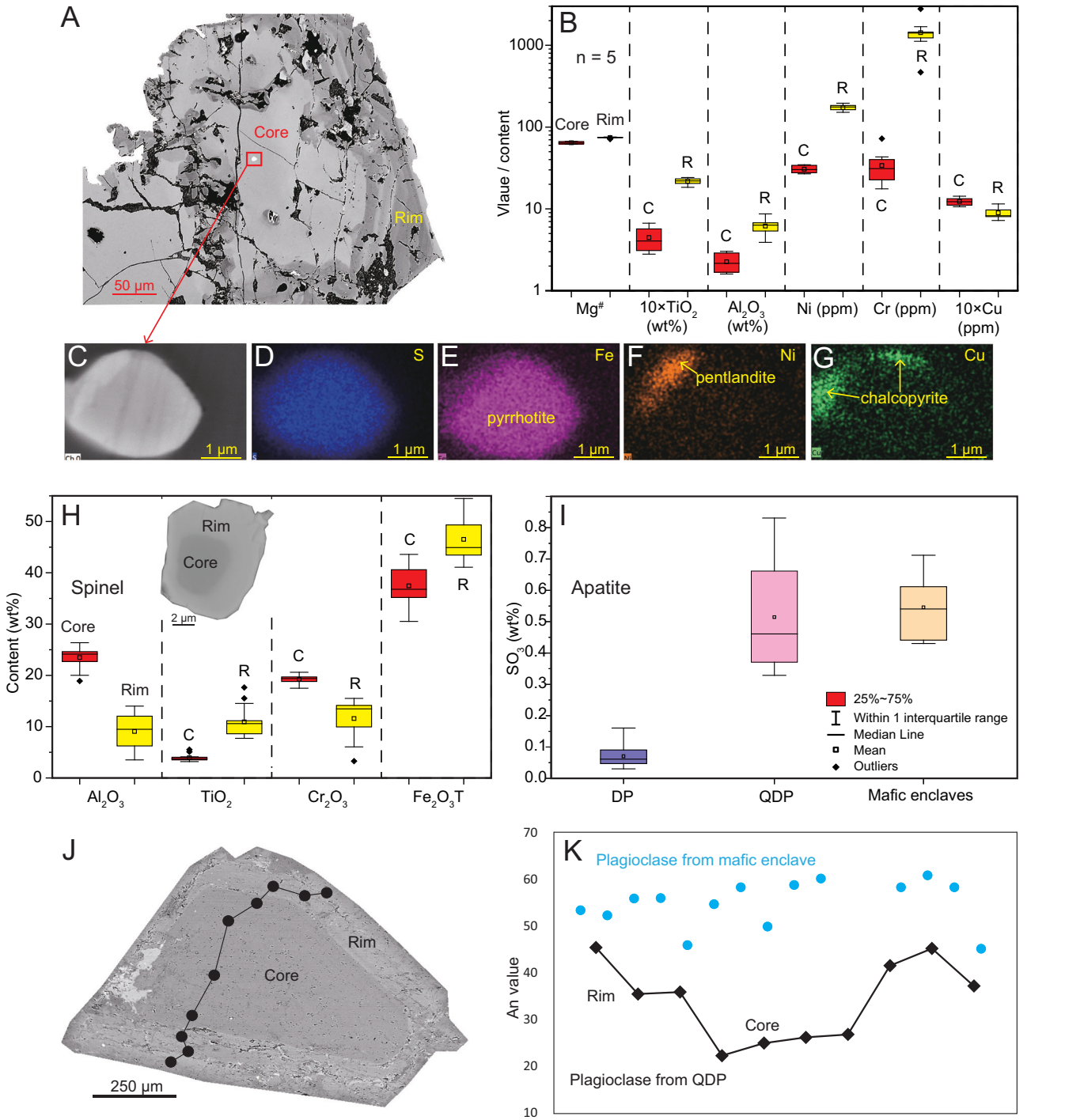

Fig. 3 | Petrographic and geochemical characteristics of minerals. A Zoned clinopyroxene from mafic enclave. **B** Major and trace elements characteristics of clinopyroxenes. **C–G** Backscattered electron (BSE) image of magmatic sulfide inclusion from the clinopyroxene core and EDS elemental mapping. **H** BSE image of spinel showing its core and rim with distinct elemental contents from mafic enclaves. **I** SO_3 content of apatites from DP, QDP and mafic enclaves. **J, K** BSE image of zoned plagioclase from QDP have an andesine rim, similar to plagioclase from mafic enclaves (blue spots are plagioclase from mafic enclaves).

abundant amphiboles. However, the pre-ore DP is reduced (ΔFMQ = +0.1 ± 0.7), which implies that amphibole fractionation had little effect on fO_2 increase. Moreover, the $(Eu/Eu^*)/Yb_N$ value of QDP is slightly higher than that of DP, suggesting an H_2O gain caused by basaltic replenishment in deep magma chambers[31]. However, the oxidation effect of this water may be limited (far below the H_2O gain oxidation trend, Fig. 2B) and cannot meet the requirements for increasing oxygen fugacity. Finally, fO_2 could increase by interaction with high fO_2 mafic magmas[18,32]. Given the zoning patterns observed in the Shaxi QDP and their absence from the Shaxi DP, we infer that the likely oxidation mechanism was interaction with an oxidized Cretaceous mafic mantle-derived melt.

The required oxidation states for sulfide-to-sulfate conversion are affected by magma composition, pressure, temperature, and H_2O content; previous experimental results provide information on typical trends[51,52]. In an empirical melt $S^{6+}/\Sigma S - fO_2$ relationship diagram (Supplementary Fig. 13A), most sulfur exists as sulfate in the oxidation states of Shaxi mafic enclaves (ΔFMQ + 2.0 to +2.6) following the experimental trachydacitic (60 to 69 wt% SiO_2) curve of Matjuschkin et al.[52] at 950 °C and ≥1 GPa

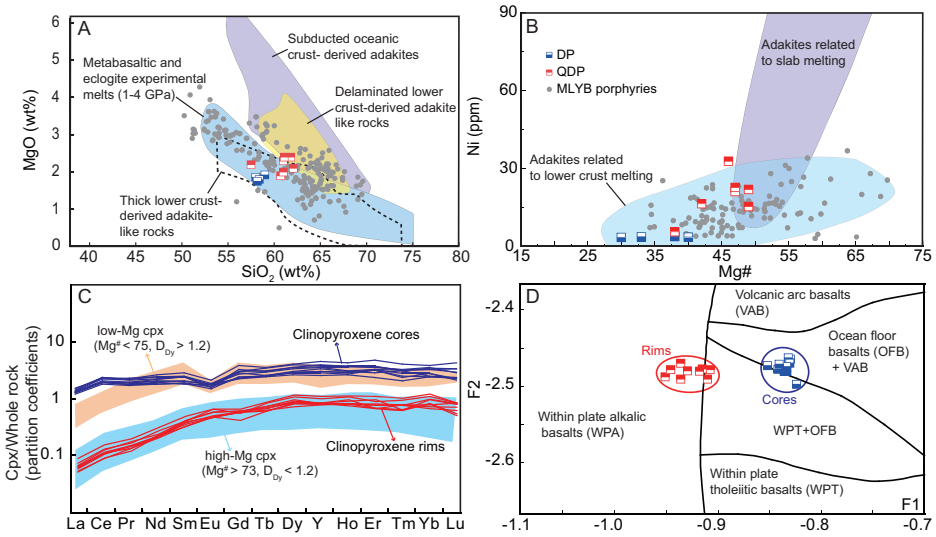

Fig. 4 | Modelling of the genetic link between Shaxi and Neoproterozoic arc magma residues. A MgO vs. SiO_2 (wt.%) diagram, **B** Ni (ppm) vs. Mg# diagrams for the Shaxi adakitic rocks (diagram modified after Wang et al. and Shen et al.)[37,90]. **C** Calculated REE clinopyroxene-melt partition coefficients for clinopyroxene cores using Shuangxiwu volcanic rocks[34] and clinopyroxene rims using Shaxi lamprophyre composition. Clinopyroxene–melt partition coefficients data for the low-Mg (brown field) and high-Mg (blue field) clinopyroxenes from Wood and Trigila[62] and Qian et al.[63]. **D** Plot of F1 against F2 for clinopyroxene (diagram modified after Nisbet and Pearce)[91].

recalculated by Nash et al.[51], according to the pressure and temperature dependence of Fe^{3+}/Fe^{2+} and the diminishing fO_2 distance between the FMQ buffer and the NNO (nickel–nickel oxide) buffer[53] reference frame used by Matjuschkin et al.[52]. Moreover, the sulfide–sulfate transformation curves will shift to the right with temperature increase and more mafic magma composition (Supplementary Fig. 13A). This also supports a mechanism of interaction with an oxidized (ΔFMQ + 2.0 to +2.6) Cretaceous mafic mantle-derived melt at 1 GPa and 1120 to 1155 °C at Shaxi. Remote stresses from long-distance paleo-Pacific plate subduction likely enhanced deep-crustal ponding of mantle-derived mafic magmas, promoting sustained thermal and chemical interaction with Proterozoic juvenile lower crust[1–5,7,9–17].

Oxidation of sulfide by ferric iron requires 8 times more mols of Fe than S: $4Fe_2O_3 + FeS = 8FeO + FeSO_4$. However, given that Fe is much more abundant in silicate melts than sulfur, even small changes in Fe^{3+} contents (e.g., an addition of 1% or 2% Fe^{3+}) are sufficient to control fO_2 and absorb electrons from most sulfide. Sulfur is often present in the hundreds to thousands of ppm, roughly one to two orders of magnitude less abundant than Fe. Indeed, recent studies[51] show that the iron-sulfur redox couple is directly correlated; a small increase in magma Fe^{3+} contents, given the much greater abundance of Fe relative to S in silicate melts, provides sufficient oxidizing capacity to drive a conspicuous increase in S^{6+} (Supplementary Fig. 13B). The variation in our spinel core-to-rim compositions suggests that the deep-sourced mafic melt supplied abundant Fe^{3+}, further supporting our model. The mafic enclaves have similar geochemical features to Cretaceous lamprophyres, derived from partial melting of a metasomatic lithospheric mantle (Supplementary Figs. 4-5), likely linked either to Neoproterozoic subduction of the Cathaysia Block beneath the Yangtze Craton[9,17,54], or to asthenospheric upwelling associated with rollback of the subducting Paleo-Pacific slab[3,55].

Source of the Neoproterozoic inherited zircons

Hafnium isotopic compositions of the DP and QDP Cretaceous zircons plot along the inferred evolution trend of Neoproterozoic inherited zircons, and show similar oxygen isotopic compositions (Fig. 2C, D; Supplementary Tables 4-5). This suggests that the Shaxi ore-forming magmas are genetically related to the protolith of the Neoproterozoic inherited zircons. The oxygen isotope composition of Cretaceous zircons from the DP and QDP is similar to that in felsic rocks in southeastern China (Fig. 2D), which have been confirmed to be derived from buried unweathered Neoproterozoic juvenile crust[11]. Moreover, inherited zircon ages are broadly coeval with the approximate peak of Neoproterozoic arc magmatism in the western Yangtze craton (ca. 813 Ma)[56], the peak crustal growth period (1000–740 Ma) of the craton[56], and the subduction of Cathaysia oceanic crust (970–840 Ma)[34]. It is difficult to precisely pinpoint the inherited zircon source, but the 850 Ma to 790 Ma Neoproterozoic magmatic rocks in the eastern Jiangnan Orogen near the MLYB[34,57] are broadly coeval with the inherited Neoproterozoic zircons from Shaxi (Fig. 1).

To test possible sources, the parent rock composition of the inherited zircons was calculated using the Smythe and Brenan method[58,59] and compared with contemporary magmatic rocks, including the Jiuling granite (822 ± 3 to 819 ± 3)[60], Xucun granite (805 ± 4 to 804 ± 7)[57], Shangshu (809 ± 14 to 731 ± 10)[57], Shuangqiaoshan (832 ± 9 to 829 ± 12)[61] rhyolites, and Shuangxiwu basaltic to andesitic volcanic rocks (1025 ± 40 to 750 ± 60)[34], all of which are located around the MLYB (Fig. 1). We used zircon-melt partition coefficients ($D_i^{zircon/melt}$) and compositions of inherited zircons to test whether calculated melt compositions are consistent with these nearby Neoproterozoic rocks. The calculated melt compositions most closely resemble those of the contemporary Shuangxiwu arc volcanic rocks (Fig. 2A, Supplementary Fig. 14)[34]. Furthermore, the trace elements of inherited zircons at Shaxi are similar to Neoproterozoic inherited zircons (830–642 Ma) in Dexing deposit (Fig. 2A), which is also believed to have been generated from Shuangxiwu arc volcanic rocks[58]. Moreover, the similar $\varepsilon_{Hf}(t)$ values (+0.0 to +4.6) of the inherited zircons and the Neoproterozoic volcanic arc rocks, together with their mantle-like oxygen isotope values (4.83–6.72‰; Supplementary Table 5), also indicate that the inherited zircons originated from arc-derived magmatic rocks (Fig. 2C, D).

REE and Y clinopyroxene–melt partition coefficients were used to derive parent melts using clinopyroxene core compositions (Mg# = 62–67) from mafic enclaves. Consistent with the zircon signature, the Shuangxiwu arc volcanic rocks emerge as the most likely source. Calculation of REE partition coefficients using the Shuangxiwu arc volcanic rocks are also similar to the reported low-Mg# (<75) mantle clinopyroxene (Fig. 4C)[62,63]. Although our measured Mg# values (62–67) of clinopyroxene cores are relatively low, they are similar to typical Mg# values of 57–70 observed in clinopyroxenes hosted in Neoproterozoic lower crust garnet–amphibolite xenoliths in the Yangtze block[6].

We can estimate clinopyroxene core formation pressures using the method of Putirka[47]. The result shows that the clinopyroxene cores crystallized at 7.6 to 12.4 kbar (average ~33 km, based on a rock density of 3.0 g cm^{-3}; Supplementary Table 6), comparable to clinopyroxene from the Neoproterozoic lower crust xenoliths in the Yangtze block (8.5—15.6 kbar)[6]. The average crustal thickness beneath the Yangtze Block is 35 km and the Jiangnan Orogen is ~40 km in the period[64]. Clinopyroxene cores plot in the volcanic arc and ocean floor basalt fields, whereas the rims plot in the within-plate field (Fig. 4D). The MLYB has no volcanic arc magmatism after subduction of the Cathaysia oceanic slab between the Cathaysia terrane and the Yangtze Craton in the Early Neoproterozoic, and there are

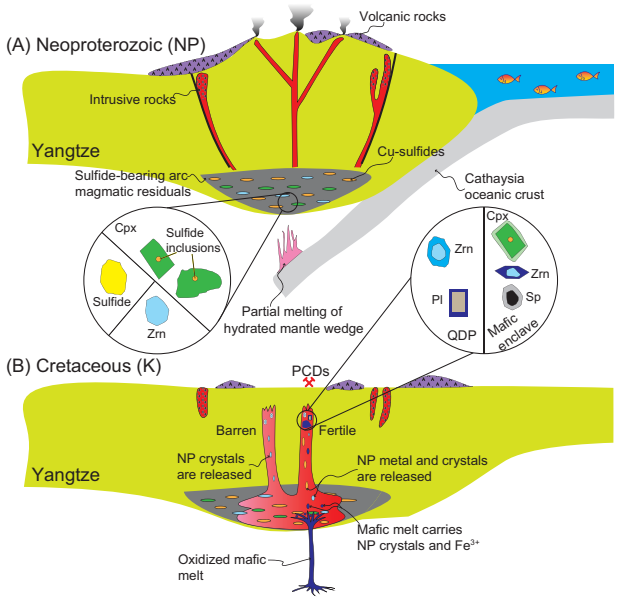

Fig. 5 | A schematic model illustrating the two suggested stages for the Shaxi PCD formation. A Sulfide-bearing arc magma residues containing clinopyroxene (Cpx) with sulfide inclusions, zircon (Zrn), sulfides, etc., formed by subduction between the Cathaysia and Yangtze blocks in the Neoproterozoic (NP), preserved at the base of the lower crust. **B** In the Cretaceous, these Neoproterozoic residues were remelted to generate the pre-ore barren DP magma with inherited NP Zrn, Cu-sulfides were then scavenged by a deep-sourced oxidized mafic melt, releasing metals (Cu, Au) to produce the fertile QDP magma with inherited NP Zrn and zoned plagioclase (Pl) and mafic enclaves with inherited NP Zrn and zoned spinel (Sp) and zoned Cpx with sulfide inclusions.

Neoproterozoic arc magma residues at the base of the crust[1–5,7,9–17], supporting a Neoproterozoic age for clinopyroxene cores. Clinopyroxenes with similar textures and compositions in Late Jurassic Xinglonggou andesites have also been shown to form from the recycling of lower continental crust[65]. Moreover, the calculated Fe–Mg exchange coefficients using the Shuangxiwu arc volcanic rocks range from 0.285 to 0.293, similar to the standard exchange coefficients (0.28 ± 0.08) derived from 1245 experimental observations[47]. Based on the clinopyroxene characteristics combined with the evolution of the tectonic setting in the MLYB, we conclude that the clinopyroxene cores from the mafic enclaves probably originated from Neoproterozoic arc-derived magmatic rocks (either the Shuangxiwu arc volcanic rocks or associated compositionally equivalent rocks; Fig. 5A).

Recycling of Neoproterozoic copper-bearing sulfides

Copper preferentially partitions into sulfides rather than silicate melts that are sufficiently sulfur-rich to have stable sulfide phases[30,49,66,67]. Moderately oxidized to reduced arc magmas (ΔFMQ < + 1.0) may become sulfide saturated during their evolution in deep magma chambers, resulting in immiscible sulfide phases that can remain suspended, or—under the right conditions—separate from the magma and form cumulates in the lower crust[23,68]. These cumulates with residual sulfide phases in the lower crust were predicted in principle and observed in rare examples of deep-arc magmatic complexes.

Experimental studies[69] suggest that neither bulk nor melt compositions have any effect on $D_{Cu}^{Cpx/melt}$, but $D_{Cu}^{Cpx/melt}$ increases with clinopyroxene Na_2O content and fO_2. Clinopyroxene Na_2O content of cores (0.57 to 0.91 wt%) and rims (0.44 to 0.81 wt%) are similar, however, the fO_2 of the source rock for the clinopyroxene cores is ΔFMQ = −1.1 ± 1.4 and that of rims is ΔFMQ = +2.3 ± 0.3. Moreover, clinopyroxene core Cu contents are higher than the rims (Fig. 3B). This suggests that the Cu content of the parental magma for the clinopyroxene cores was higher than Cu in the parental magma for their rims. Copper contents of the parental magma of the Neoproterozoic arc-derived magmatic rocks and mantle-derived mafic magma have been estimated using the Cu content of clinopyroxenes in the mafic enclaves and $D_{Cu}^{Cpx/melt}$ (Cu partition coefficient for Cpx/melt)[69]. Accounting for the analytical error and the oxidation state, we use the minimum (0.017 ± 0.002) and maximum (0.105 ± 0.054) of $D_{Cu}^{Cpx/melt}$ with Na_2O content between 0 and 1 wt% from the Liu et al.[69] experiments to estimate the parental magma Cu contents of clinopyroxene cores and rims, respectively.

Calculation of the parental magma of the Neoproterozoic inherited zircons and clinopyroxene cores suggests that the Cu contents of their parental magmas were 56 to 95 ppm (Supplementary Table 7), which is comparable to the initial Cu content (40–60 ppm)[49,70] of magma believed to generate porphyry Cu deposits in the thick continental crust. This is a minimum number, because sulfide saturation causes Cu depletion during the evolution of the arc magma[49,67,71]. It is consistent with high Cu and Au contents (~125 ppm Cu, ~68 ppb Au)[72] in Shuangxiwu arc volcanic rocks, and is higher than the lower continental crust of Eastern China (46 ppm Cu)[73].

Copper contents for the Cretaceous mafic magmas calculated using clinopyroxene rims (5–23 ppm; Supplementary Table 7) generated from either asthenospheric or lithospheric mantle are similar or lower than the primitive mantle (20–35 ppm)[74,75]. Therefore, it is unlikely that the mafic magmas on their own could generate a PCD, but this provides additional evidence for the metal being derived from Neoproterozoic sulfide-bearing residues. Modeling for Cu concentrations of melts also implies that the Shuangxiwu arc volcanic rocks are good candidates for the source of magmas parental to the Shaxi deposit, but must interact with a high fO_2 mafic magma (Supplementary Fig. 15).

Implications

The Cu contents of Neoproterozoic arc volcanic rocks in the Jiangnan orogen range from initial values of ~60 ppm at 9.0 wt% MgO (similar to Cu content in thicker arcs and MORB)[76] and steadily increase to maximum values of ~200 ppm at ~6.0 wt% MgO, then decrease sharply (Supplementary Fig. 16). This suggests that the magmas were sulfide-saturated following the onset of magnetite crystallization. It has been suggested that magnetite fractionation causes a decrease in fO_2 and Fe contents in arc magmas, which further promotes sulfide saturation[71,77]. The onset of the decrease in Cu contents in arc magmas depends on the thickness of the crust and generally starts at 5–10 wt.% MgO in thicker arcs and 4–6 wt.% MgO in thinner arcs, which supports that a large amount of Cu sequestered in the former accumulates as copper sulfides within or at the base of thicker arcs[70,76] (Fig. 5A). Magnetite coexists with sulfides in melt inclusions hosted in clinopyroxene cores (Supplementary Fig. 7), establishing the link between sulfide saturation and magnetite fractionation. Elevated sulfide saturation caused by assimilation of reduced crust or magnetite fractionation is generally considered detrimental to the genesis of syn-magmatic PCDs because it limits the flux of ore-forming elements to shallow crustal levels[6,23,43–45].

The sulfide-bearing residues generated by this process would act as an important reservoir and source of ore-forming materials for subsequent magmatic events to generate fertile magmas parental to non-arc PCDs[6,8,18,20,25,70]. However, if there is no suitable trigger mechanism during the remelting of the sulfide-bearing residues, the sulfide cannot oxidize to sulfate, and the ore-forming metals cannot be released. Therefore, an increase in fO_2 is crucial during the remelting of the sulfide-bearing residues, such that ore-forming metals are subsequently released to generate PCD ore-forming magmas (Fig. 5B). Modeling for Cu concentrations of melts implies that the Shuangxiwu arc volcanic rocks are good candidates for the source of magmas parental to Shaxi deposit, but must interact with a high fO_2 mafic magma. A similar process has been observed in modern volcanic systems, suggesting that it may also be applied to older porphyry systems[78].

Our study provides direct evidence in support of the hypothesis that the sulfide-bearing residues generated by the arc magmas during ascent and evolution through the crust can act as an important reservoir and source of ore-forming materials in the non-arc settings (Fig. 5A). Although the metals

(e.g., Cu) content of magmas that forms typical PCDs does not need to be particularly high[79], it is clear that the more metal that magmas can transfer to the exsolved fluids[18,22,25], the larger the PCDs that can be formed by later hydrothermal activity. Exceptionally high fO_2 (ΔFMQ = +0.8 to +3.0) ultrapotassic magmas have also been confirmed to be involved in the post-subduction porphyry mineralization process in Tibet[32,80]. As such, new mafic magma with high fO_2 generated by magmatic activity in non-arc settings may well be required for the formation of this mineralization type worldwide (Fig. 5B).

Methods

Whole-rock geochemistry

Major and trace element analyses of representative, least-altered intrusive rocks from the Shaxi deposit were carried out at ALS Chemex (Guangzhou), China. For major elements, ~0.9 g of calcined or ignited powder was fused with ~9.0 g of a 1:1 mixture of lithium tetraborate and lithium metaborate at 1050–1100 °C in an autofluxer. The resulting glass disk was analyzed using X-ray fluorescence, with analytical uncertainties of approximately ±1–2%. For trace elements, ~0.2 g of powdered sample was fused with ~0.9 g lithium metaborate at 1000 °C, and the glass bead was subsequently dissolved in 4% HNO_3. Trace element concentrations were determined by inductively coupled plasma-mass spectrometry (ICP-MS), with precision better than ±5% for most elements.

Electron probe microanalysis (EPMA)

Analyses of apatite and plagioclase were conducted at the Central Science Laboratory, University of Tasmania, using a Cameca SX100 instrument. Operating conditions included an accelerating voltage of 15 kV, a beam current of 10 nA, and a spot size of 10 µm, with a takeoff angle of 40°. Analytical uncertainties for most elements were within 1%. Clinopyroxene analyses were carried out on the same model instrument at the Microbeam Laboratory, University of Manitoba, under 15 kV accelerating voltage and a 20 nA focused beam with a 10 µm diameter. Detection limits for major elements (Na, Mg, Al, Si, Cl, K, Ca, Mn, Fe) were typically better than 0.1%. Counting times were 15 s for peaks and 5 s for backgrounds. All data were corrected using standard ZAF matrix procedures.

Clinopyroxene and apatite trace element analyses

Trace element concentrations were measured by laser ablation inductively coupled plasma mass spectrometry (LA-ICP-MS) at the Ore Deposit and Exploration Centre (ODEC), Hefei University of Technology, China. Analyses employed an Agilent 7900 quadrupole ICP-MS coupled to a Photon Machines Analyte HE 193 nm ArF excimer laser equipped with a SQUID signal-smoothing device. Helium was used as the carrier gas and mixed with argon make-up gas via a T-connector prior to entering the ICP. A spot diameter of 30 µm was used, with an 8 Hz repetition rate, ~2 J/cm^2 fluence, and 40 s ablation following a 20 s gas blank. Calibration was based on external standards (GSE-1g, BCR-2G, NIST 610, NIST 612), using preferred values from the GeoReM database (http://georem.mpch-mainz.gwdg.de/). Data reduction was performed offline using the ICPMS DataCal software. Analytical uncertainties are estimated at ~5% for major elements and ~10% for trace elements.

Zircon U–Pb isotope and trace element analyses

Zircons were separated from drill core samples and analyzed at the University of Tasmania, Hobart, using an Agilent 7500cs quadrupole ICP-MS coupled to a 193 nm Coherent ArF excimer laser with a Resonetics S155 ablation cell. Downhole fractionation, instrument drift, and mass bias for Pb/U ratios were corrected using two analyses of the primary standard (91500) and one analysis of each secondary standard (Temora and JG1) at the start of each session and every 15 unknown zircons (~30 min intervals) under the same spot size and conditions as the samples. Additional secondary standards (Mud Tank, Penglai, and Plešovice zircons) were also analyzed. Correction factors for $^{207}Pb/^{206}Pb$ ratios were determined from large NIST610 spots measured every 30 unknowns and adjusted following Baker et al.[81]. Each zircon was ablated at 32 µm spot size, 5 Hz repetition rate, and ~2 J/cm^2 fluence, preceded by a 30 s blank and followed by 30 s of signal acquisition. Helium carrier gas at 0.35 L/min transported ablated material to the plasma, mixed with argon make-up gas before entering the torch. Isotopes measured included ^{49}Ti, ^{56}Fe, ^{90}Zr, ^{178}Hf, ^{202}Hg, ^{204}Pb, ^{206}Pb, ^{207}Pb, ^{208}Pb, ^{232}Th, and ^{238}U, with 0.16 s dwell per element and longer counting times for Pb isotopes. Zircon element abundances were calculated using Zr as the internal standard, assuming stoichiometric proportions, with mass bias and drift corrected using NIST610.

Zircon O isotopes

Oxygen isotopic analyses of zircons were performed at the Australian National University (ANU), Canberra, using a SHRIMP II equipped with a Cs source and an electron gun for charge compensation following Ickert et al.[82]. Analyses were conducted on 20 µm spots in multiple collector mode, using an axial continuous electron multiplier (CEM) triplet collector and two floating heads with interchangeable CEM-Faraday cups. The Temora II reference zircon was analyzed to monitor and correct for isotope fractionation, with measured $^{18}O/^{16}O$ ratios normalized to a weighted mean $\delta^{18}O$ of +8.2‰[82]. Reproducibility for Temora II $\delta^{18}O$ was ±0.55 to 0.72‰ (2σ). Secondary reference zircons from the Duluth Gabbro sample FC1 yielded $\delta^{18}O$ values of 5.41 ± 0.35‰ and 5.42 ± 0.62‰ (2σ).

Zircon Lu–Hf isotopes

LA-MC-ICP-MS analyses of zircon Lu-Hf isotopes were conducted at the Australian National University (ANU), Canberra, following SHRIMP $^{18}O/^{16}O$ measurements. Analyses used a 193 nm excimer laser-based HELEX ablation system coupled to a Neptune multiple-collector ICP-MS, with a 41 µm spot size and ablation times up to 60 s. Accepted $^{176}Hf/^{177}Hf$ values for zircon standards were taken from Sláma et al.[83] and Woodhead and Hergt[84]. Single-stage model ages (T_{DM}) were calculated using measured $^{176}Lu/^{177}Hf$ ratios relative to a $^{176}Hf/^{177}Hf$ ratio of 0.28325 and a $^{176}Lu/^{177}Hf$ of 0.0384 for a depleted mantle model. Two-stage model ages (T_{DM2}) for the magma source were calculated assuming a mean $^{176}Lu/^{177}Hf$ of 0.015 for average continental crust.

Data availability

All the data used for this study are available in Supplementary Tables 1–12 or through Figshare (at https://figshare.com/s/9432716b9f91679c14b5).

Received: 10 April 2024; Accepted: 24 September 2025;
Published online: 07 November 2025

References

1. Bi, H. et al. Seismic evidence for a transcrustal magmatic pathway contributing to critical metal deposits. *Geophys. Res. Lett.* **51**, https://doi.org/10.1029/2023gl104935 (2024).
2. Chen, L., Zheng, Y.-F. & Zhao, Z.-F. A common crustal component in the sources of bimodal magmatism: Geochemical evidence from Mesozoic volcanics in the Middle-Lower Yangtze Valley, South China. *GSA Bull.* https://doi.org/10.1130/b31856.1 (2018).
3. Chen, L., Zheng, Y.-F. & Zhao, Z.-F. Origin of arc-like magmatism at fossil convergent plate boundaries: geochemical insights from Mesozoic igneous rocks in the Middle to Lower Yangtze Valley, South China. *Earth-Sci. Rev.* **211**, 103416 (2020).
4. Hou, J. et al. The deep background of large-scale, Mesozoic Cu-Au-W metallogenesis in northeastern South China: constraints from Yingshan-Changshan wide-angle seismic reflection/refraction data. *Sci. China Earth Sci.* **65**, 2202–2218 (2022).
5. Hou, Z. et al. Lithosphere architecture characterized by crust-mantle decoupling controls the formation of orogenic gold deposits. *Natl Sci. Rev.* **10**, nwac257 (2023).
6. Hou, Z. et al. Recycling of metal-fertilized lower continental crust: Origin of non-arc Au-rich porphyry deposits at cratonic edges. *Geology* **45**, 563–566 (2017).

7. Pirajno, F. & Zhou, T. Intracontinental porphyry and porphyry-skarn mineral systems in Eastern China: scrutiny of a special case "Made-in-China". *Econ. Geol.* **110**, 603–629 (2015).
8. Richards, J. P. Postsubduction porphyry Cu-Au and epithermal Au deposits: Products of remelting of subduction-modified lithosphere. *Geology* **37**, 247–250 (2009).
9. Tang, M. et al. Neoproterozoic subducted materials in the generation of Mesozoic Luzong volcanic rocks: evidence from apatite geochemistry and Hf–Nd isotopic decoupling. *Gondwana Res.* **21**, 266–280 (2012).
10. Wang, X.-L. et al. Evolution of deep crustal hot zones constrained by the diversity of Late Mesozoic magmatic rocks in SE China. *Ore Geol. Rev.* **134**, https://doi.org/10.1016/j.oregeorev.2021.104143 (2021).
11. Xu, H., Wang, X.-L. & Guan, Y. Mantle-like to low oxygen isotopes in zircon from the mid-Cretaceous high-silica granites reveal unweathered basement recycling along the present coastal area of SE China. *Lithos* **466-467**, https://doi.org/10.1016/j.lithos.2023.107465 (2024).
12. Yang, Z. & Cooke, D. Porphyry copper deposits in China. *Soc. Econ. Geol. Spec. Publ.* **22**, 133–187 (2019).
13. Zhang, H. et al. Seismically imaged lithospheric delamination and its controls on the Mesozoic Magmatic Province in South China. *Nat. Commun.* **14**, 2718 (2023).
14. Zhang, Y. et al. The crustal and uppermost mantle vs structure of the middle and lower reaches of the Yangtze River metallogenic belt: implications for metallogenic process. *J. Geophys. Res. Solid Earth* **128**, https://doi.org/10.1029/2023jb026817 (2023).
15. Zhang, Z.-Y. et al. Crustal architectural controls on critical metal ore systems in South China based on Hf isotopic mapping. *Geology* **51**, 738–742 (2023).
16. Zheng, Y. et al. Hydrothermal ore deposits in collisional orogens. *Sci. Bull.* **64**, 205–212 (2019).
17. Zhou, T. et al. A review of the intracontinental porphyry deposits in the Middle-Lower Yangtze River Valley metallogenic belt, Eastern China. *Ore Geol. Rev.* **65**, 433–456 (2015).
18. Wilkinson, J. J. Triggers for the formation of porphyry ore deposits in magmatic arcs. *Nat. Geosci.* **6**, 917–925 (2013).
19. Zheng, Y.-C. et al. Cu isotopes reveal initial Cu enrichment in sources of giant porphyry deposits in a collisional setting. *Geology* **47**, 135–138 (2018).
20. Pettke, T., Oberli, F. & Heinrich, C. A. The magma and metal source of giant porphyry-type ore deposits, based on lead isotope microanalysis of individual fluid inclusions. *Earth Planet. Sci. Lett.* **296**, 267–277 (2010).
21. Griffin, W. L., Begg, G. C. & O'Reilly, S. Y. Continental-root control on the genesis of magmatic ore deposits. *Nat. Geosci.* **6**, 905–910 (2013).
22. Core, D. P., Kesler, S. E. & Essene, E. J. Unusually Cu-rich magmas associated with giant porphyry copper deposits: evidence from Bingham, Utah. *Geology* **34**, https://doi.org/10.1130/g21813.1 (2006).
23. Tassara, S. & Ague, J. J. A role for crustal assimilation in the formation of copper-rich reservoirs at the base of continental arcs. *Econ. Geol.* **117**, 1481–1496 (2022).
24. Holwell, D. A. et al. A metasomatized lithospheric mantle control on the metallogenic signature of post-subduction magmatism. *Nat. Commun.* **10**, 3511 (2019).
25. Holwell, D. A. et al. Mobilisation of deep crustal sulfide melts as a first order control on upper lithospheric metallogeny. *Nat. Commun.* **13**, 573 (2022).
26. Richards, J. P. & Şengör, A. M. C. Did Paleo-Tethyan anoxia kill arc magma fertility for porphyry copper formation?. *Geology* **45**, 591–594 (2017).
27. Zhang, J., Wang, R. & Hong, J. Amphibole fractionation and its potential redox effect on arc crust: evidence from the Kohistan arc cumulates. *Am. Mineral.* **107**, 1779–1788 (2022).
28. Tang, M., Lee, C. A., Ji, W. Q., Wang, R. & Costin, G. Crustal thickening and endogenic oxidation of magmatic sulfur. *Sci. Adv.* **6**, eaba6342 (2020).
29. Tang, M., Erdman, M., Eldridge, G. & Lee, C. A. The redox "filter" beneath magmatic orogens and the formation of continental crust. *Sci. Adv.* **4**, eaar4444 (2018).
30. Lee, C.-T. A. & Tang, M. How to make porphyry copper deposits. *Earth Planet. Sci. Lett.* **529**, 115868 (2020).
31. Loucks, R. R. & Fiorentini, M. L. Oxidation of magmas during gain and loss of H_2O recorded by trace elements in zircon. *Earth Planet. Sci. Lett.* **622**, https://doi.org/10.1016/j.epsl.2023.118377 (2023).
32. Li, W. et al. Redox state of southern Tibetan upper mantle and ultrapotassic magmas. *Geology* **48**, 733–736 (2020).
33. Zhao, G. Jiangnan Orogen in South China: developing from divergent double subduction. *Gondwana Res.* **27**, 1173–1180 (2015).
34. Li, X.-H. et al. Amalgamation between the Yangtze and Cathaysia Blocks in South China: constraints from SHRIMP U–Pb zircon ages, geochemistry and Nd–Hf isotopes of the Shuangxiwu volcanic rocks. *Precambrian Res.* **174**, 117–128 (2009).
35. Chang, Y., Liu, X. & Wu, Y. *The Copper-iron Belt of the Lower and Middle Reaches of the Changjiang River* (Geology Publication House, Beijing, 71p, 1991).
36. Li, H. et al. Geochemical and zircon U–Pb study of the Huangmeijian A-type granite: implications for geological evolution of the Lower Yangtze River belt. *Int. Geol. Rev.* **53**, 499–525 (2010).
37. Wang, Q. et al. Petrogenesis of Cretaceous adakitic and shoshonitic igneous rocks in the Luzong area, Anhui Province (eastern China): implications for geodynamics and Cu–Au mineralization. *Lithos* **89**, 424–446 (2006).
38. Wang, S. et al. Ore genesis and hydrothermal evolution of the Shaxi porphyry Cu–Au deposit, Anhui province, Eastern China: evidence from isotopes (S–Sr–H–O), pyrite, and fluid inclusions. *Miner. Depos.* **56**, 767–788 (2020).
39. Loucks, R. R., Fiorentini, M. L. & Henríquez, G. J. New magmatic oxybarometer using trace elements in zircon. *J. Petrol.* **61**, egaa034 (2020).
40. Zhang, X.-N. et al. Diagnostic REE patterns of magmatic and hydrothermal apatite in the Zhuxi tungsten skarn deposit, China. *J. Geochem. Explor.* **252**, https://doi.org/10.1016/j.gexplo.2023.107271 (2023).
41. Xu, W. et al. Mafic microgranular enclaves formed by gas-driven filter pressing during rapid cooling: an example from the Gangdese Batholith in Southern Tibet. *J. Petrol.* **61**, https://doi.org/10.1093/petrology/egab003 (2020).
42. Li, H. et al. Basalt derived from highly refractory mantle sources during early Izu-Bonin-Mariana arc development. *Nat. Commun.* **12**, 1723 (2021).
43. Konecke, B. A., Fiege, A., Simon, A. C., Parat, F. & Stechern, A. Co-variability of S^{6+}, S^{4+}, and S^{2-} in apatite as a function of oxidation state: Implications for a new oxybarometer. *Am. Mineralogist* **102**, 548–557 (2017).
44. Kleinsasser, J. M. et al. Sulfide and sulfate saturation of dacitic melts as a function of oxygen fugacity. *Geochim. Cosmochim. Acta* **326**, 1–16 (2022).
45. Parat, F., Holtz, F. & Klügel, A. S-rich apatite-hosted glass inclusions in xenoliths from La Palma: constraints on the volatile partitioning in evolved alkaline magmas. *Contrib. Mineral. Petrol.* **162**, 463–478 (2011).
46. Georgatou, A. A. & Chiaradia, M. Magmatic sulfides in high-potassium calc-alkaline to shoshonitic and alkaline rocks. *Solid Earth* **11**, 1–21 (2020).
47. Putirka, K. D. Thermometers and barometers for volcanic systems. *Rev. Mineral. Geochem.* **69**, 61–120 (2008).
48. Hao, H., Campbell, I. H., Richards, J. P., Nakamura, E. & Sakaguchi, C. Platinum-group element geochemistry of the Escondida igneous suites, Northern Chile: implications for ore formation. *J. Petrol.* **60**, 487–514 (2019).
49. Park, J.-W., Campbell, I. H., Chiaradia, M., Hao, H. & Lee, C.-T. Crustal magmatic controls on the formation of porphyry copper deposits. *Nat. Rev. Earth Environ.* **2**, 542–557 (2021).

50. Tatnell, L., Anenburg, M. & Loucks, R. Porphyry copper deposit formation: identifying garnet and amphibole fractionation with REE pattern curvature modeling. *Geophys. Res. Lett.* **50**, https://doi.org/10.1029/2023gl103525 (2023).
51. Nash, W. M., Smythe, D. J. & Wood, B. J. Compositional and temperature effects on sulfur speciation and solubility in silicate melts. *Earth Planet. Sci. Lett.* **507**, 187–198 (2019).
52. Matjuschkin, V., Blundy, J. D. & Brooker, R. A. The effect of pressure on sulphur speciation in mid- to deep-crustal arc magmas and implications for the formation of porphyry copper deposits. *Contrib. Mineral. Petrol.* **171**, https://doi.org/10.1007/s00410-016-1274-4 (2016).
53. Kress, V. C. & Carmichael, I. S. E. The compressibility of silicate liquids containing Fe_2O_3 and the effect of composition, temperature, oxygen fugacity and pressure on their redox states. *Contrib. Mineral. Petrol.* **108**, 82–92 (1991).
54. Yang, Z.-Y. & Jiang, S.-Y. Diverse lamprophyres origins corresponding to lithospheric thinning: a case study in the Jiurui district of Middle-Lower Yangtze River Belt, South China Craton. *Gondwana Res.* **54**, 62–80 (2018).
55. Meng, X. et al. Contrasting tectonomagmatic conditions for coexisting iron oxide-apatite deposits and porphyry and Skarn Cu ± Au deposits in the Middle-Lower Yangtze River Metallogenic Belt, China. *Econ. Geol.* **119**, 1059–1087 (2024).
56. Sun, W.-H. et al. Detrital zircon U–Pb geochronological and Lu–Hf isotopic constraints on the Precambrian magmatic and crustal evolution of the western Yangtze Block, SW China. *Precambrian Res.* **172**, 99–126 (2009).
57. Wang, X.-L. et al. Post-orogenic extension in the eastern part of the Jiangnan orogen: Evidence from ca 800–760Ma volcanic rocks. *Precambrian Res.* **222-223**, 404–423 (2012).
58. Zhang, C.-C. et al. Oxygen fugacity and porphyry mineralization: A zircon perspective of Dexing porphyry Cu deposit, China. *Geochim. Cosmochim. Acta* **206**, 343–363 (2017).
59. Smythe, D. J. & Brenan, J. M. Magmatic oxygen fugacity estimated using zircon-melt partitioning of cerium. *Earth Planet. Sci. Lett.* **453**, 260–266 (2016).
60. Xin, Y. et al. Neoproterozoic post-collisional extension of the central Jiangnan Orogen: geochemical, geochronological, and Lu-Hf isotopic constraints from the ca. 820–800 Ma magmatic rocks. *Precambrian Res.* **294**, 91–110 (2017).
61. Li, L. et al. Ca. 830 Ma back-arc type volcanic rocks in the eastern part of the Jiangnan orogen: Implications for the Neoproterozoic tectonic evolution of South China Block. *Precambrian Res.* **275**, 209–224 (2016).
62. Wood, B. J. & Trigila, R. Experimental determination of aluminous clinopyroxene–melt partition coefficients for potassic liquids, with application to the evolution of the Roman province potassic magmas. *Chem. Geol.* **172**, 213–223 (2001).
63. Qian, Q. et al. Variations of clinopyroxene/melt element partitioning during assimilation of olivine/peridotite by low-Mg diorite magma. *Chem. Geol.* **419**, 36–54 (2015).
64. Zhang, Y. et al. The crustal thickness and composition in the eastern South China Block constrained by receiver functions: Implications for the geological setting and metallogenesis. *Ore Geol. Rev.* **130**, 103988 (2021).
65. Gao, S. et al. Recycling lower continental crust in the North China craton. *Nature* **432**, 892–897 (2004).
66. Rottier, B., Chelle-Michou, C., Casanova, V., Pastore, C. & Tollan, P. Early Au-rich sulfide liquid saturation explains the low Au endowment of continental intraplate alkaline magmas. *Geology* **50**, 1409–1414 (2022).
67. Hao, H., Campbell, I. H., Park, J.-W. & Cooke, D. R. Platinum-group element geochemistry used to determine Cu and Au fertility in the Northparkes igneous suites, New South Wales, Australia. *Geochim. Cosmochim. Acta* **216**, 372–392 (2017).
68. Tomkins, A. G., Rebryna, K. C., Weinberg, R. F. & Schaefer, B. F. Magmatic sulfide formation by reduction of oxidized arc basalt. *J. Petrol.* **53**, 1537–1567 (2012).
69. Liu, X. et al. Partitioning of copper between olivine, orthopyroxene, clinopyroxene, spinel, garnet and silicate melts at upper mantle conditions. *Geochim. Cosmochim. Acta* **125**, 1–22 (2014).
70. Chiaradia, M. Copper enrichment in arc magmas controlled by overriding plate thickness. *Nat. Geosci.* **7**, 43–46 (2014).
71. Jenner, F. E., O'Neill, H. S. T. C., Arculus, R. J. & Mavrogenes, J. A. The magnetite crisis in the evolution of arc-related magmas and the initial concentration of Au, Ag and Cu. *J. Petrol.* **51**, 2445–2464 (2010).
72. Ma, D. & Liu, Y. Geochemical characteristics and genesis of stratabound gold deposits in Jiangnan gold metallogenic belt. *Sci. China Ser. B* **35**, 240–256 (1992).
73. Gao, S. et al. Structure and composition of the continental crust in East China. *Sci. China Ser. D Earth Sci.* **42**, 129–140 (1999).
74. Palme, H. & O'Neill, H. S. C. Cosmochemical estimates of mantle composition. In *Treatise on Geochemistry* 1–39 (2014).
75. McDonough, W. F. & Sun, S. S. The composition of the Earth. *Chem. Geol.* **120**, 223–253 (1995).
76. Lee, C. T. et al. Copper systematics in arc magmas and implications for crust-mantle differentiation. *Science* **336**, 64–68 (2012).
77. Sun, W., Arculus, R. J., Kamenetsky, V. S. & Binns, R. A. Release of gold-bearing fluids in convergent margin magmas prompted by magnetite crystallization. *Nature* **431**, 975–978 (2004).
78. Audétat, A. & Simon, A. C. Magmatic controls on porphyry copper genesis. *Soc. Econ. Geol. Spec. Publ.* **16**, 553–572 (2012).
79. Richards, J. P. The oxidation state, and sulfur and Cu contents of arc magmas: implications for metallogeny. *Lithos* **233**, 27–45 (2015).
80. Xu, B. et al. Mercury isotope evidence for the importance of recycled fluids in collisional ore systems. *Sci. Adv.* **10**, eadp7383 (2024).
81. Baker, J., Peate, D., Waight, T. & Meyzen, C. Pb isotopic analysis of standards and samples using a ^{207}Pb–^{204}Pb double spike and thallium to correct for mass bias with a double-focusing MC-ICP-MS. *Chem. Geol.* **211**, 275–303 (2004).
82. Ickert, R. B. et al. Determining high precision, in situ, oxygen isotope ratios with a SHRIMP II: Analyses of MPI-DING silicate-glass reference materials and zircon from contrasting granites. *Chem. Geol.* **257**, 114–128 (2008).
83. Sláma, J. et al. Plešovice zircon — a new natural reference material for U–Pb and Hf isotopic microanalysis. *Chem. Geol.* **249**, 1–35 (2008).
84. Woodhead, J. D. & Hergt, J. M. A preliminary appraisal of seven natural zircon reference materials for in situ Hf isotope determination. *Geostand. Geoanal. Res.* **29**, 183–195 (2005).
85. He, C., Dong, S., Santosh, M. & Chen, X. Seismic evidence for a geosuture between the Yangtze and Cathaysia Blocks, South China. *Sci. Rep.* **3**, 2200 (2013).
86. Sano, Y., Terada, K. & Fukuoka, T. High mass resolution ion microprobe analysis of rare earth elements in silicate glass, apatite and zircon: lack of matrix dependency. *Chem. Geol.* **184**, 217–230 (2002).
87. Cottrell, E. et al. Oxygen fugacity across tectonic settings. In *Magma Redox Geochemistry* 33–61 (2021).
88. Chen, Z. et al. Petrogenesis of keratophyes in the Pingshui Group, Zhejiang: constraints from zircon U-Pb ages and Hf isotopes. *Sci. Bull.* **54**, 1570–1578 (2009).
89. Yin, C. et al. Tectonic evolution of the southeastern margin of the Yangtze Block: constraints from SHRIMP U-Pb and LA-ICP-MS Hf isotopic studies of zircon from the eastern Jiangnan Orogenic Belt and implications for the tectonic interpretation of South China. *Precambrian Res.* **236**, 145–156 (2013).
90. Shen, Y. et al. Petrology of the Machangqing Complex in Southeastern Tibet: implications for the genesis of potassium-rich adakite-like intrusions in collisional zones. *J. Petrol.* **62**, https://doi.org/10.1093/petrology/egab066 (2021).

91. Nisbet, E. G. & Pearce, J. A. Clinopyroxene composition in mafic lavas from different tectonic settings. *Contrib. Mineral. Petrol.* **63**, 149–160 (1977).

Acknowledgements
This work was financially supported by the National Natural Science Foundation of China (42172078, 91962218, 41702071), and the National Key R&D Program of China (2016YFC0600206). M.A. was supported by Australian Research Council Linkage grant LP190100785. No specific permissions were required for the collection of samples. We sincerely thank the Editor, Santiago Tassara, and the two anonymous reviewers for their valuable comments, which greatly improved the manuscript. Special thanks to Professor Noel White and Professor José Piquer for their guidance during the revision process.

Author contributions
S.-W.W. designed the project, performed analyses, and wrote and revised the manuscript. T.-F.Z. discovered the Neoproterozoic zircons. M.A. contributed to data interpretation, manuscript writing, and revision. P.H. designed clinopyroxene EPMA analyses and interpreted the data. L.-J.Z. designed zircon dating and elemental analyses and interpreted the zircon data. Y.F. performed sample collection and whole-rock analyses. D.R.C. contributed to zircon data interpretation. B.F. designed the Hf-O isotopic analytical method and collected the data.

Competing interests
The authors declare no competing interests.

Additional information
Supplementary information The online version contains supplementary material available at https://doi.org/10.1038/s43247-025-02830-z.

Correspondence and requests for materials should be addressed to Shiwei Wang or Michael Anenburg.

Peer review information *Communications Earth and Environment* thanks Santiago Tassara and the other, anonymous, reviewer(s) for their contribution to the peer review of this work. Primary Handling Editors: David Hernández Uribe, Joe Aslin and Carolina Ortiz Guerrero. [A peer review file is available.]